J. Fluid Mech. (1987), *vol.* 177, *pp.* 265–292
Printed in Great Britain

Vortex-driven acoustically coupled combustion instabilities

By THIERRY J. POINSOT, ARNAUD C. TROUVE, DENIS P. VEYNANTE, SEBASTIEN M. CANDEL† AND EMILE J. ESPOSITO

Laboratoire E.M2.C, CNRS et Ecole Centrale des Arts et Manufactures,
Chatenay-Malabry, France

(Received 15 January 1986 and in revised form 15 July 1986)

Combustion instability is investigated in the case of a multiple inlet combustor with dump. It is shown that low-frequency instabilities are acoustically coupled and occur at the eigenfrequencies of the system. Using spark-schlieren and a special phase-average imaging of the C_2-radical emission, the fluid-mechanical processes involved in a vortex-driven mode of instability are investigated. The phase-average images provide maps of the local non-steady heat release. From the data collected on the combustor the processes of vortex shedding, growth, interactions and burning are described. The phases between the pressure, velocity and heat-release fluctuations are determined. The implications of the global Rayleigh criterion are verified and a mechanism for low-frequency vortex-driven instabilities is proposed.

1. Introduction

Many types of combustion instabilities have been investigated in the past thirty years. These phenomena occur in many practical systems such as power plants, ramjets or afterburners. They enhance heat transfer rates at the combustor walls and induce vibrations of large amplitude. In extreme cases, important structural damage and loss of control of the power plant or propulsion system may occur.

When such phenomena are encountered in the development of a system, the usual practice is to follow a process of trial and error with the objective of suppressing or at least reducing the instability. The large number of mechanisms involved in unstable combustion and their complexity (turbulence, acoustics, chemical kinetics, vibrations) make difficult any systematic prevision of instability for a given system. Recent research in this field has been directed to better description and understanding of the basic mechanisms of instability in combustion systems. In many cases acoustic processes play a determining role in the unstable mechanism, and the existence of eigenmodes of the combustion cavity is often related to the appearance of unstable combustion. This class of acoustically coupled combustion instabilities has received considerable attention (see Barrere & Williams 1968; Putnam 1971; Harrje & Reardon 1972; Williams 1985, for reviews of this subject). While numerous studies concern the acoustic features of unstable combustion processes, much less is known on the fluid-mechanical mechanisms involved and on the response of the flame to acoustic oscillations. There is, however, experimental evidence indicating that these aspects are of considerable importance. In many unstable combustion situations the

---

† Also with ONERA, BP 72, 92322 Chatillon, France.

flow features large-scale organized motions with the appearance of coherent periodic patterns.

An early indication of the importance of vortices in combustion instability phenomena is given by Rogers & Marble (1956) in a study of high-frequency oscillations in ramjets and afterburners. These authors show that under screeching combustion a transverse acoustic mode is excited in the duct. This mode produces large sloshing velocities in the vicinity of the flameholder lips. These fluctuations trigger the shedding of vortices. Fresh mixture is entrained by the vortices and transported into the hot wake of the stabilizer. After a certain characteristic time the vortices burn and the heat pulse produced feeds energy into the transverse acoustic mode. The process may then repeat itself periodically if certain phasing conditions are satisfied.

In the more recent experiment of Keller *et al.* (1981) (see also Parker, Sawyer & Ganji 1979; Pitz & Daily 1981) many modes of instabilities are made evident. These modes involve large-scale motions of the flame front. Under certain operating conditions intense acoustic modes are excited and the flame front rolls up into large periodic vortices. Another experiment performed by Smith & Zukoski (1985) on a system with dump (sudden expansion) provides important clues on vortex-driven acoustic instabilities. In this experiment, vortex shedding from the rear edge of the flame holder is associated with the cyclic (plane) acoustic oscillations in the combustor. The vortex grows, entraining fresh mixture into hot combustion products in the wake of the step. When the vortex reaches the combustor wall, intense mixing and burning takes place. The heat pulse produced in this process generates a pressure wave. The velocity fluctuation associated with this wave triggers the shedding of a new vortex and the process is thus repeated periodically.

Other types of large-scale flame-front motion have been observed in experiments performed on ducted flames. In a detailed study by Blackshear (1958) acoustic disturbances of different frequencies were injected through the flame stabilizer. Large motions with a vortical character were observed at various frequencies.

More recent experiments by Bray *et al.* (1983) and Yamaguchi, Ohiwa & Hasegawa (1985) concern low-frequency motions ('buzz' in the terminology of these authors) in which flames stabilized on single or multiple rods develop large breathing oscillations. This motion may lead to the separation of the flam into lumps.

Thus it is clear that in many cases combustion instabilities involve large-scale oscillations of the flame front. In certain cases the amplitude of the motion becomes so large that the flame front rolls up into periodic discrete vortices. These vortices play a decisive role in the mechanism of instability.

To improve our understanding of this mechanism it is necessary to study how the vortices form, grow, interact, burn and couple to other modes of oscillation of the combustor. Now, the information which is least available from most earlier studies concerns the process of non-steady heat release. Little is known on the space–time variation of the rate of reaction. This information is not directly accessible from schlieren photographs.

In the present study we shall use in addition to schlieren photography an imaging method for the determination of the local instantaneous rate of reaction. The method is based on the detection of C_2-radical light emission in combination with phase-average imaging (PAI). It provides the local heat release in the combustor at different times of the instability cycle. This is achieved by synchronizing the data acquisition on a reference pressure signal.

A comparison between schlieren photographs and phase-average images of C_2

radiation yields quantitative information on the growth and evolution of the flame in the vortex. The process by which energy is fed into the unstable oscillation is thus described.

To complete the analysis of the phenomena it is also necessary to examine the feedback processes taking place in the combustor. The nature of these processes is not unique. In many circumstances acoustic waves are involved. In the present case, the identification of the feedback process is based on a one-dimensional analysis of the acoustic mode structure in the system.

Based on these tools near our analysis concerns an intense mode of instability associated with the cyclic formation of large coherent vortices shed at the inlet plane of the combustor. The vortices dominate the flow field in the reactive zone and they induce a large-amplitude periodic heat-release component. The experiment is performed in a multiple-inlet dump combustor (a sudden expansion cavity). One advantage of this configuration is that it allows a study of mutual interactions between adjacent vortex patterns. In contrast to single-step dump combustors and V-gutter ducted flames considered in the literature, our configuration is less influenced by boundary effects like cooling or friction.

The experimental configuration is described in §2. The phase-average imaging is presented in §3. Section 4 gives an analysis of the acoustic-mode structure of the system in the low-frequency range. The resonant modes and the corresponding eigenfrequencies calculated on this basis are given in §5. A comparison with experimental observations allows an identification of the feedback processes. A vortex-driven acoustic instability is described in §6 with schlieren and phase-averaging images. Finally a mechanism for this type of instability is proposed in §7.

2. Experimental configuration

The experimental configuration is displayed in figure 1. A mixture of air and propane is injected through a long duct into a dump combustor. The combustor has a square section of 100×100 mm^2 and is 200 mm long. The inlet plane comprises five narrow injection slots separated by four backward-facing steps. Two half-steps separate the first and last slots from the lateral walls. Each slot has a rectangular cross-section of 3×100 mm^2 and the blockage is 85 %. The combustor walls are made of ceramic and they are surrounded by a layer of insulating material. A stainless-steel structure holds these parts together. In designing this combustor our objective was to dispense with the use of water cooling and to approach adiabatic combustion conditions. The combustor sidewalls are equipped with two air-cooled circular quartz windows. These windows have a diameter of 40 mm and their axis is located on the centreline 21 mm from the inlet plane. They allow a direct examination of the flame structure and they are also used for schlieren imaging and C_2 radical emission detection. Acoustic measurements are performed on the test duct located on the upstream side of the combustor. This duct has a rectangular cross-section of 110×130 mm^2 and it is 1200 mm long. Sixteen instrumentation ports allow pressure measurements. Two of the ports are connected to a pair of JBL 24/82 driver units. These units may be used to drive pressure oscillations into the system. In the present experiments these devices were not used and a single B & K 4135 microphone was employed to measure the pressure signal in the test duct. This microphone (M_1) was placed 0.38 m from the combustor inlet plane. Further details on the combustion facility and many test results may be found in Darabiha (1984).

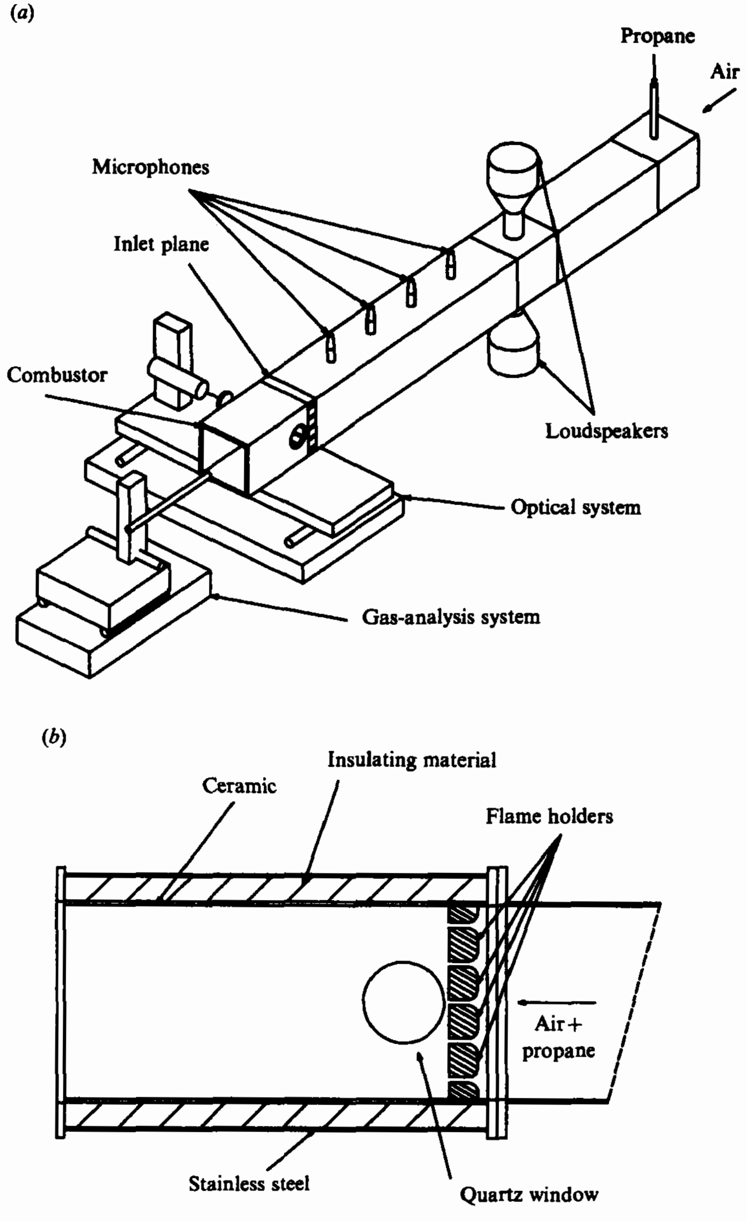

FIGURE 1. (*a*) Experimental apparatus; (*b*) combustor configuration.

3. Time-resolved optical measurements and phase-average imaging

3.1. C_2-*radical light emission*

In studies of combustion instabilities it is important to obtain information on the non-steady energy release processes. These processes drive the combustor oscillations and their characteristic time is equal to the period of the cyclic fluctuations.

Exact time-resolved measurements of the local energy release are not available, but many observations indicate that the light radiated by the combustion zone is

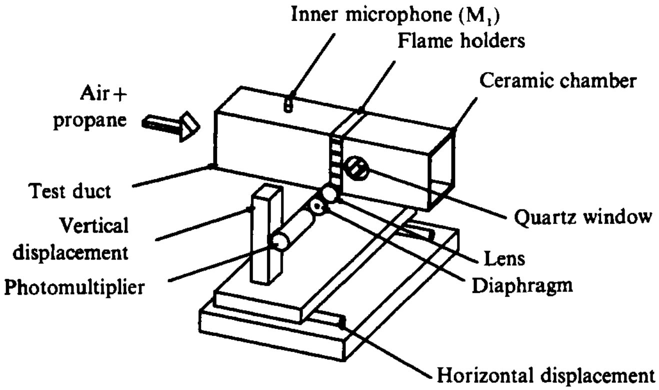

FIGURE 2. Optical instrumentation.

related to the reaction intensity and hence to the heat-release process. Now, certain free radicals like C_2, CH, OH appear almost exclusively in the reactive zones and their concentration is always small. Hence, the self-absorption of the light emitted by these radicals is not important, and the radiated light intensity is then directly related to the reaction rate, or equivalently, to the heat-release rate. Early studies of John & Summerfield (1957) and John, Wilson & Summerfield (1955) indicate that the radiation of free radicals like C_2 and CH is indeed meaningful in this respect. These authors show that the ratio of the light intensities emitted by CH and C_2 radicals is a function of the fuel/air ratio at the point of observation (the ratio of the mass flow rate of fuel to the mass flow rate of air).

In a more recent study of sound emission by flames, Hurle *et al.* (1968) establish a correlation between the C_2 or CH radical emission in a narrow band and the volumetric heat-release rate. By changing the air flow rate and the equivalence ratio, they show that the C_2 emission intensity is directly proportional to the volume consumption of the mixture. The linear relation remains true for both laminar and turbulent flow regimes.

Another indirect proof of this relation is provided by experiments performed on soap bubbles filled with a combustible ethylene–air mixture. When the soap bubble is ignited and its contents burn, a sound wave is radiated. The sound pressure at a distance from the bubble is proportional to the time derivative of the heat-release term $\mathrm{d}Q/\mathrm{d}t$. Now, it is shown by Hurle *et al.* (1968) that this quantity may be deduced by simply differentiating the light intensity emitted by free radicals like C_2 or CH: $\mathrm{d}Q/\mathrm{d}t = k\,\mathrm{d}I/\mathrm{d}t$. The sound pressure waveform may be predicted on this basis, and it is remarkably close to the waveform detected in the experiment.

The linear relation between the free-radical light emission and the heat-release source term has not been proved in many flow configurations but it may be safely concluded that a monotonic relation exists between these two quantities.

Our estimation of the heat-release source term relies on this assumption. The emission band used to this purpose is the $(0,0)\,C_2$ band at a wavelength $\lambda = 5165$ Å. This wavelength is isolated in the emission spectrum with a narrowband interferential filter ($\Delta\lambda \approx 50$ Å).

The optical arrangement is shown in figure 2. The light emitted by the flame is collected by an $f = 54$ mm convex lens placed at about 100 mm from the combustor central plane. The light beam is then filtered and the filtered light intensity is detected

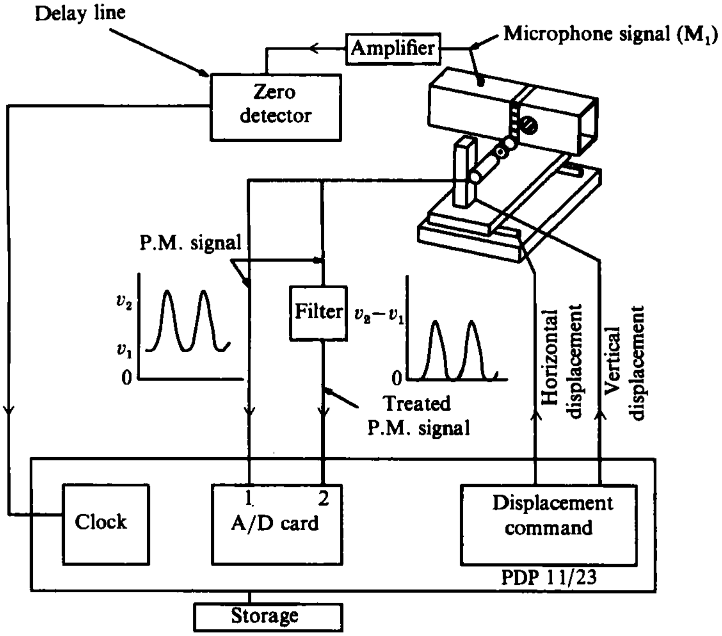

FIGURE 3. Phase-average imaging (PAI) method.

by a 'La Radiotechnique' XP1002 photomultiplier through a 1 mm diameter pinhole to provide a local measurement: the emitting area actually seen by the photomultiplier has a diameter of 0.8 mm. The detector output is amplified, low-pass filtered to prevent aliasing and transmitted to a PDP 11/23 computer through an 8-channel, 12-bit A/D converter. This first signal contains the continuous and fluctuating components, respectively corresponding to the steady and non-steady heat-release terms. Now it is worth extracting the fluctuating component from the complete signal. This is achieved by subtracting the pedestal of the photomultiplier output (see figure 3). This second signal is then amplified, low-pass filtered and transmitted to the computer through a second channel of the A/D converter.

3.2. *Phase-average imaging*

The photomultiplier is displaced on a predetermined grid of $41 \times 41 = 1681$ points encompassing the quartz windows. At each point x of this grid the data acquisition is synchronized with respect to the pressure signal detected by microphone M_1. The zero crossings of this signal are recognized and a delay line delivers a triggering signal to the PDP 11/23 clock (see figure 3). If T_k designates the kth triggering moment then the fluctuating-intensity data samples acquired at a constant rate from this initial moment are

$$f_k(l) = f(x, l\Delta t + T_k) \quad \text{for } k = 0, \ldots, N-1, \quad l = 0, \ldots, L-1. \tag{1}$$

In this expression Δt designates the sampling period, N is the number of cycles examined and L is the number of samples acquired in each cycle.

A standard time average may be formed with these samples:

$$\bar{f} = \frac{1}{NL} \sum_{k=0}^{N-1} \sum_{l=0}^{L-1} f_k(l). \tag{2}$$

A phase average or conditioned average may also be defined by summing samples corresponding to the same moment in each cycle over all cycles:

$$\langle f(l)\rangle = \frac{1}{N}\sum_{k=0}^{N-1} f_k(l). \tag{3}$$

With this definition the fluctuating signal detected by the photomultiplier may be written in the form

$$f(\boldsymbol{x},t) = \langle f\rangle + f', \tag{4}$$

where f' represents the fluctuations of the signal around the phase average.

In some applications the signal f is decomposed into three terms:

$$f(\boldsymbol{x},t) = \bar{f}+\tilde{f}+f', \tag{5}$$

where $\tilde{f}$ is obtained by subtracting the standard average from the periodic average $\langle f\rangle$ ($\tilde{f} = \langle f\rangle - \bar{f}$). This representation is not adopted here. We shall only consider the phase average $\langle f\rangle$. The measurements described in the paper are performed by acquiring $L = 9$ data points per cycle at a sampling period $\Delta t = 0.23$ ms and averaging these samples over $N = 100$ cycles.

3.3. *Spark-schlieren visualization*

Spark-schlieren photographs are also synchronized with respect to the same pressure signal. The photographs are obtained at nine different moments in the cycle separated by a constant time interval of $\Delta t = 0.23$ ms, thus allowing a direct comparison with the C_2 phase-average emission maps. The spark duration is less than 30 ns in order to 'freeze' the flow structure and obtain sharp schlieren exposures (at the mean flow speed of 50 m/s the displacement of a particle is less than 1 μm during the spark 30 ns).

4. Low-frequency modal analysis

The acoustic feedback processes involved in combustion instability may be identified from modal analysis. When the frequency of the combustion oscillation is less than the first cut-off frequency $f_c(1,0)$ characterizing the first (1,0) transverse acoustic mode of the system, it is known that all higher modes are evanescent. Under such circumstances the acoustic field consists of plane waves. Now, consider one particular duct section characterized by a flow Mach number M, a mean density ρ and a sound speed c. At this location one of the plane waves propagates in the positive axial direction (in the downstream direction) with a wavenumber $k_+ = k/(1+M)$, while another plane wave propagates in the negative axial direction (in the upstream direction) with a wavenumber $k_- = -k/(1-M)$. The acoustic pressure and velocity fields are then described by the following expressions:

$$\left.\begin{aligned} p(\boldsymbol{x},t) &= A_+ e^{i(k_+ x-\omega t)} + A_- e^{i(k_- x-\omega t)}, \\ v(\boldsymbol{x},t) &= \frac{A_+}{\rho c} e^{i(k_+ x-\omega t)} - \frac{A_-}{\rho c} e^{i(k_- x-\omega t)}, \end{aligned}\right\} \tag{6}$$

where A_+, A_- designate the complex amplitudes of the downstream- and upstream-travelling waves and ω is the angular frequency.

This field representation may be applied to a system formed by duct segments of variable cross-section and variable flow characteristics by defining N sub-elements.

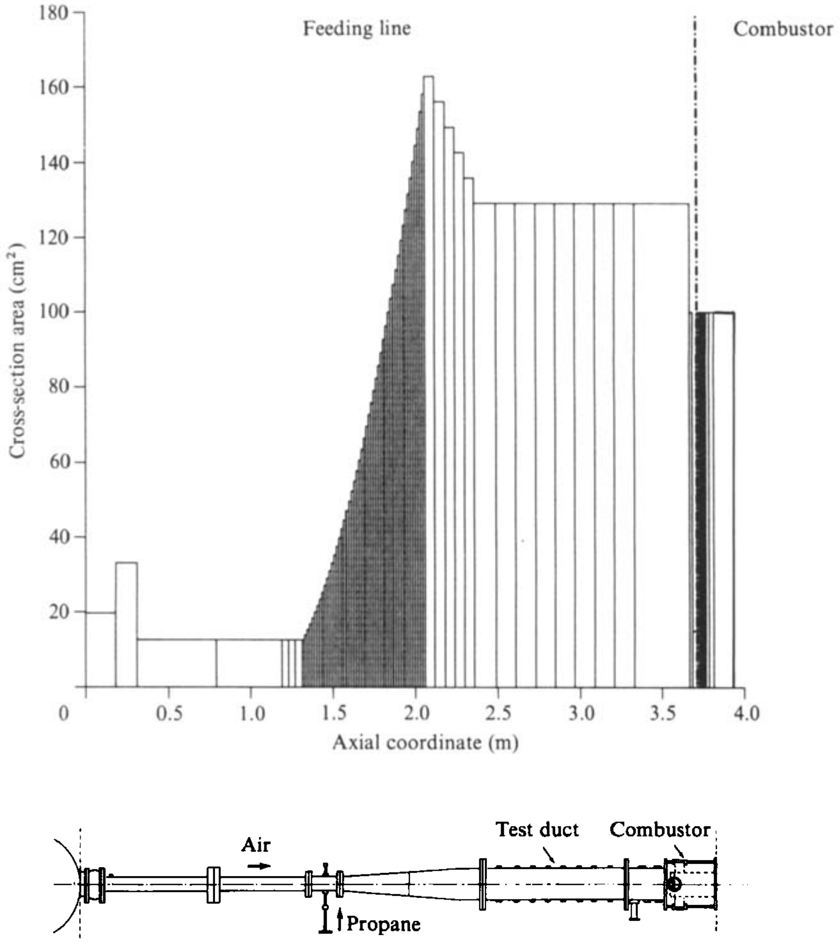

FIGURE 4. Area distribution in the discretized system.

In each sub-element, the flow characteristics and the cross-section must remain approximately constant. This 'finite-element' subdivision is exemplified in figure 4. This figure displays the area distribution in the combustion facility and the sub-elements used to represent this facility. The first element starts at the large settling tank located upstream. The last element terminates at the combustor exhaust. Ten elements are used to account for the temperature and density changes in the combustor cavity.

At this point of the analysis the influence of vortices and non steady heat release on the acoustic field is neglected. Combustion is involved in the determination of the acoustic field only through the variations it induces on mean temperature and consequently on mean density and sound speed distributions. As far as the calculation of the system low resonance frequencies is concerned, the pressure waves are assumed to be plane even in the combustion chamber and the flame zone may be viewed as a local acoustic source.

This one-dimensional assumption is justified by the 'compactness' of the reaction zone: typically, the acoustic wavelength of the main modes occurring during combustion is about 0.9 m (the frequencies of these modes lie between 400 and

600 Hz), while the reaction-zone length does not exceed 8 cm (this length is determined from an examination of the mean flow structure obtained from gas analysis; see Darabiha *et al.* 1985).

Let the subscript j identify the parameters pertaining to the jth element. With this notation $l_j, S_j, \rho_j, c_j, M_j$ respectively designate the length, cross-section, density, sound speed and Mach number of this element. The left-boundary of the jth element located at x_j constitutes the interface between the jth and the $(j-1)$th element.

With these definitions the acoustic field in the jth element may be expressed in the following form:

$$\left.\begin{aligned} p_j(\boldsymbol{x}, t) &= [A_{j+}\,\mathrm{e}^{\mathrm{i}k_{j+}(x-x_j)} + A_{j-}\,\mathrm{e}^{\mathrm{i}k_{j-}(x-x_j)}]\,\mathrm{e}^{-\mathrm{i}\omega t}, \\ v_j(\boldsymbol{x}, t) &= \left[\frac{A_{j+}}{\rho_j c_j}\mathrm{e}^{\mathrm{i}k_{j+}(x-x_j)} - \frac{A_{j-}}{\rho_j c_j}\mathrm{e}^{\mathrm{i}k_{j-}(x-x_j)}\right]\mathrm{e}^{-\mathrm{i}\omega t}. \end{aligned}\right\} \tag{7}$$

Now, effects of flow Mach number on wave propagation are neglected ($M \approx 0.02$ in the upstream duct and $M \approx 0.05$ in the combustor). These effects may be safely neglected, and hence $k_{j+} = -k_{j-} = k_j$.

By matching the pressure and volume flow rates across the jth interface a transfer matrix is obtained which relates the plane wave amplitudes in two successive elements:

$$\begin{bmatrix} A_{(j+1)+} \\ A_{(j+1)-} \end{bmatrix} = \frac{1}{2}\begin{bmatrix} \mathrm{e}^{\mathrm{i}k_{j+}}\rho_j(1+\beta_j) & \mathrm{e}^{\mathrm{i}k_{j-}}\rho_j(1-\beta_j) \\ \mathrm{e}^{\mathrm{i}k_{j+}}\rho_j(1-\beta_j) & \mathrm{e}^{\mathrm{i}k_{j-}}\rho_j(1+\beta_j) \end{bmatrix}\begin{bmatrix} A_{j+} \\ A_{j-} \end{bmatrix} \tag{8}$$

where β_j represents the ratio of the specific impedances per unit duct area:

$$\beta_j = \left(\left(\rho_{j+1}\frac{c_{j+1}}{\rho_j c_j}\right)\frac{S_j}{S_{j+1}}\right).$$

Figure 4 provides the area distribution corresponding to the experimental set-up.

Now, let $\boldsymbol{T}_j$ designate the transfer matrix appearing in (8); then $S^N = \prod_{j=1}^{N-1} \boldsymbol{T}_j$ is the global transfer matrix of the system and it relates the wave amplitudes in the first and last elements:

$$\begin{bmatrix} A_{N+} \\ A_{N-} \end{bmatrix} = \begin{bmatrix} S_{11}^N & S_{12}^N \\ S_{21}^N & S_{22}^N \end{bmatrix}\begin{bmatrix} A_{1+} \\ A_{1-} \end{bmatrix}. \tag{9}$$

Boundary conditions at the system inlet and outlet yield two other relations which may be written in the general form

$$A_{1+}/A_{1-} = R_1, \quad A_{N+}/A_{N-} = R_N. \tag{10}$$

The set of relations (9), (10) is only satisfied if the characteristic function

$$F = (S_{11}^N R_1 + S_{12}^N) - R_N(S_{21}^N R_1 + S_{22}^N) \tag{11}$$

vanishes. This condition determines the eigenfrequencies of the system. The corresponding eigenmodes are obtained by arbitrarily fixing one wave amplitude in a particular sub-element (for example setting A_{1-}) and calculating all other amplitudes from (8) and (10).

Various degrees of refinement may be used in the specification of the boundary conditions (10). In the present situation the inlet and outlet may be described as pressure nodes. The reflection factors R_1 and R_N are then given by

$$R_1 = -1, \quad R_N = -\mathrm{e}^{\mathrm{i}(k_{1-}-k_{1+})\,l_N}. \tag{12}$$

Computed frequencies (Hz)		Measured frequencies (Hz)
37	393	390
105	443	440
128	488	485
184	535	530
220	589	590
256	633	
306	681	
343	731	
	777	

Table 1. Computed longitudinal eigenfrequencies of the system and measured frequencies ($f < 800$ Hz)

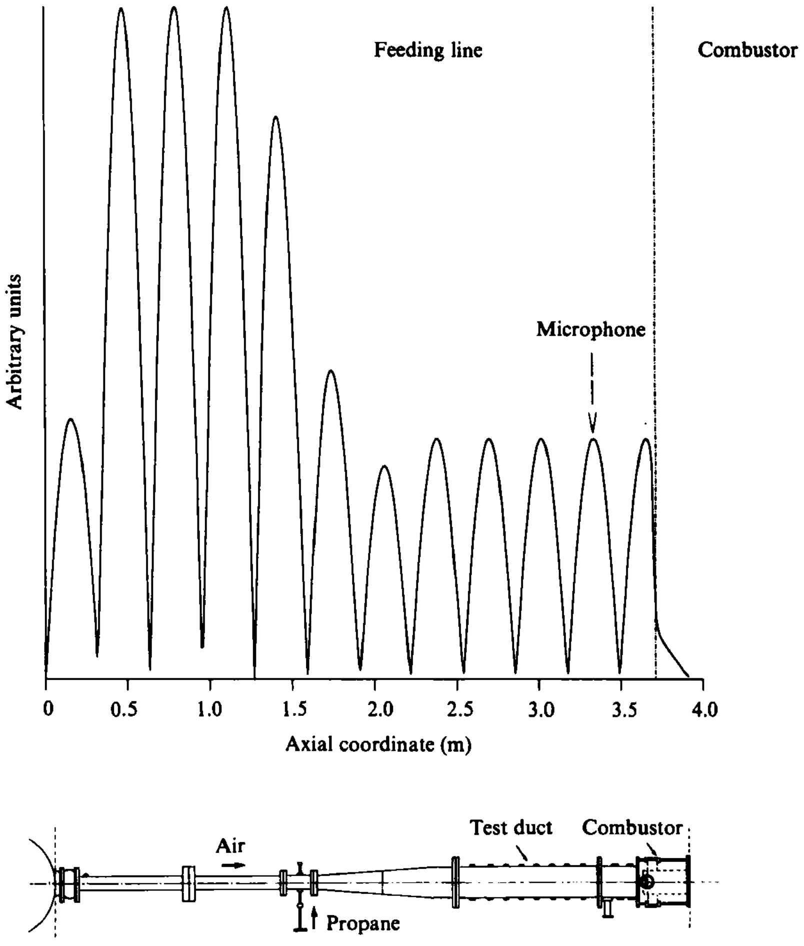

Figure 5. Modal structure of the 535 Hz acoustic eigenfrequency.

5. Acoustic-mode identification

5.1. *Results of calculations*

The calculations performed to determine the acoustic modes of the combustion facility rely on the theory described in the previous section and use the discretization and area distribution shown in figure 4. The temperature in each element is obtained from experimental data. The pressure is assumed to be constant and equal to the ambient. The density and sound speed are determined from perfect-gas expressions. The temperature and area distributions thus allow a complete determination of the specific impedance ratios β_j for all the sub-elements composing the system. The eigenfrequencies of the first 17 plane modes of the system are shown in table 1. These frequencies are not regularly distributed because the system has a variable cross-section and non-uniform density and sound-speed characteristics. The mean separation between successive eigenfrequencies is about 45 Hz. The amplitude of a typical eigenmode corresponding to $f = 535$ Hz is shown in figure 5. This mode has been selected because it appears in the most unstable regime of the system. The modal structure is relatively complex. It exhibits 12 maxima. There is no pressure node inside the combustor cavity. The microphone M_1 placed on the test duct detects the pressure oscillations at the second antinode.

5.2. *Experimental observations*

An experimental exploration of the flow regimes may be accomplished by varying the air flow rate and the equivalence ratio Φ (defined as the fuel/air ratio divided by the fuel/air ratio under stoichiometric conditions). Acoustic monitoring, mean-flow gas analysis and schlieren observations indicate that there are two main types of regimes. The following description summarizes the results of Darabiha *et al.* (1985):

For low values of the equivalence ratio $\Phi < 0.8$ (for lean mixtures) the combustion regime is smooth and stable, the sound pressure level observed in the upstream duct is low and the pressure fluctuations have a broadband spectrum with a few discrete peaks. The mean-flow structure is not periodic: the two lower jets interact and combine, the two inner jets form another single jet while the upper jet remains isolated and bends towards the upper sidewall. Spark-schlieren photographs (see figure 6) show a normal turbulent mixing and spreading of the fresh-mixture jets.

For higher values of the equivalence ratio $\Phi > 0.8$ (for mixtures approaching stoichiometric conditions) the combustion regime is unstable, the sound pressure level is increased and discrete peaks in the spectrum become predominant. In this situation a preferred mode of oscillation is excited and concentrates most of the acoustic power. The main frequencies observed are listed in table 1. Intense oscillations are found at 440, 485, 530 and 590 Hz. A typical power spectral density of microphone M_1 is displayed in figure 7. This spectrum corresponds to the 530 Hz regime.

Measured and calculated frequencies are in agreement, clearly identifying the acoustic contribution to the combustion instability and the modes involved in the process. It is worth indicating that all calculated acoustic frequencies do not appear during combustion: the characteristic times of convection and combustion processes in the flow determine a range of possible frequencies where coupling may occur. In our experiment, the eight lowest acoustic frequencies were out of this range and never appeared. The same result holds true for acoustic frequencies higher than 600 Hz.

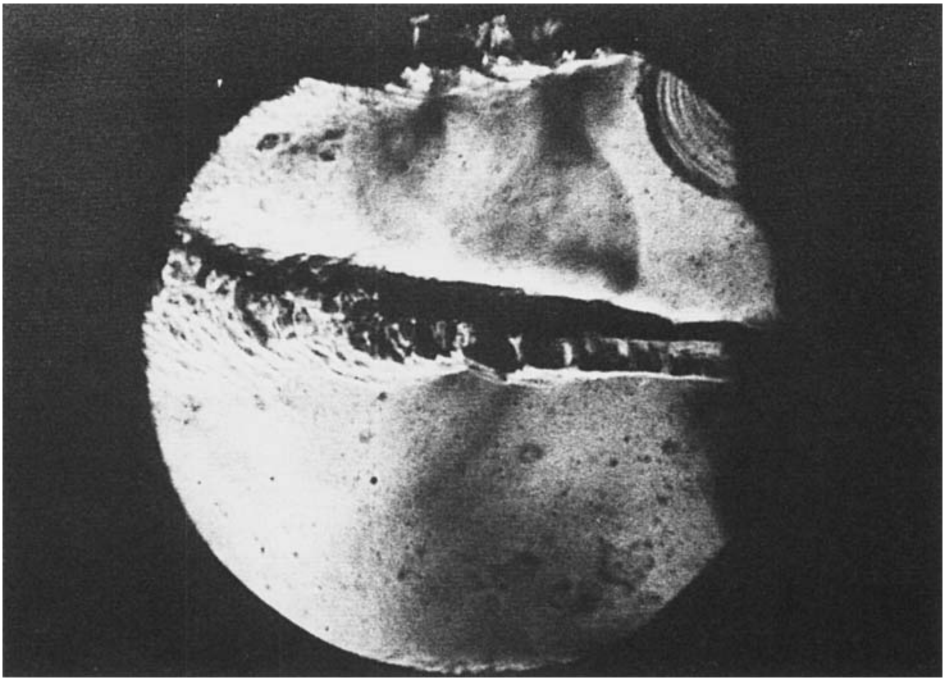

FIGURE 6. Spark-schlieren photograph of the central jet for a typical stable regime. $\dot{m}_{\rm air} = 87$ g/s, $\Phi = 0.72$.

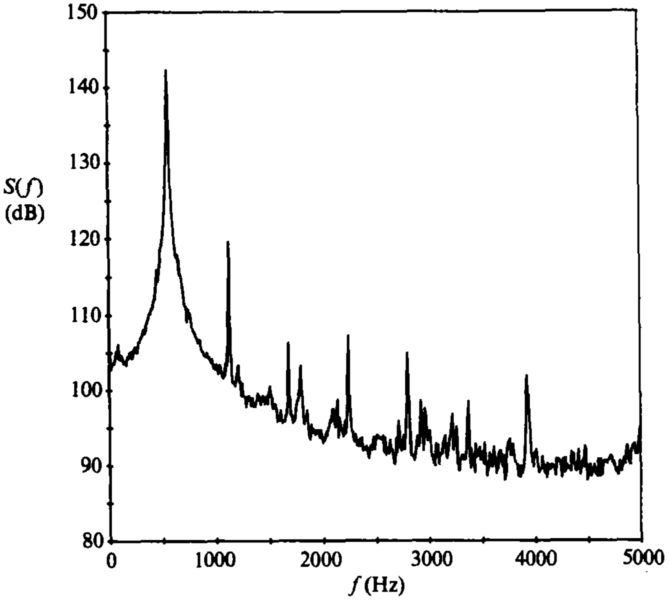

FIGURE 7. Power spectral density of microphone M_1 for an unstable combustion regime. $\dot{m}_{\rm air} = 78$ g/s, $\Phi = 0.83$. Peak frequency: 530 Hz.

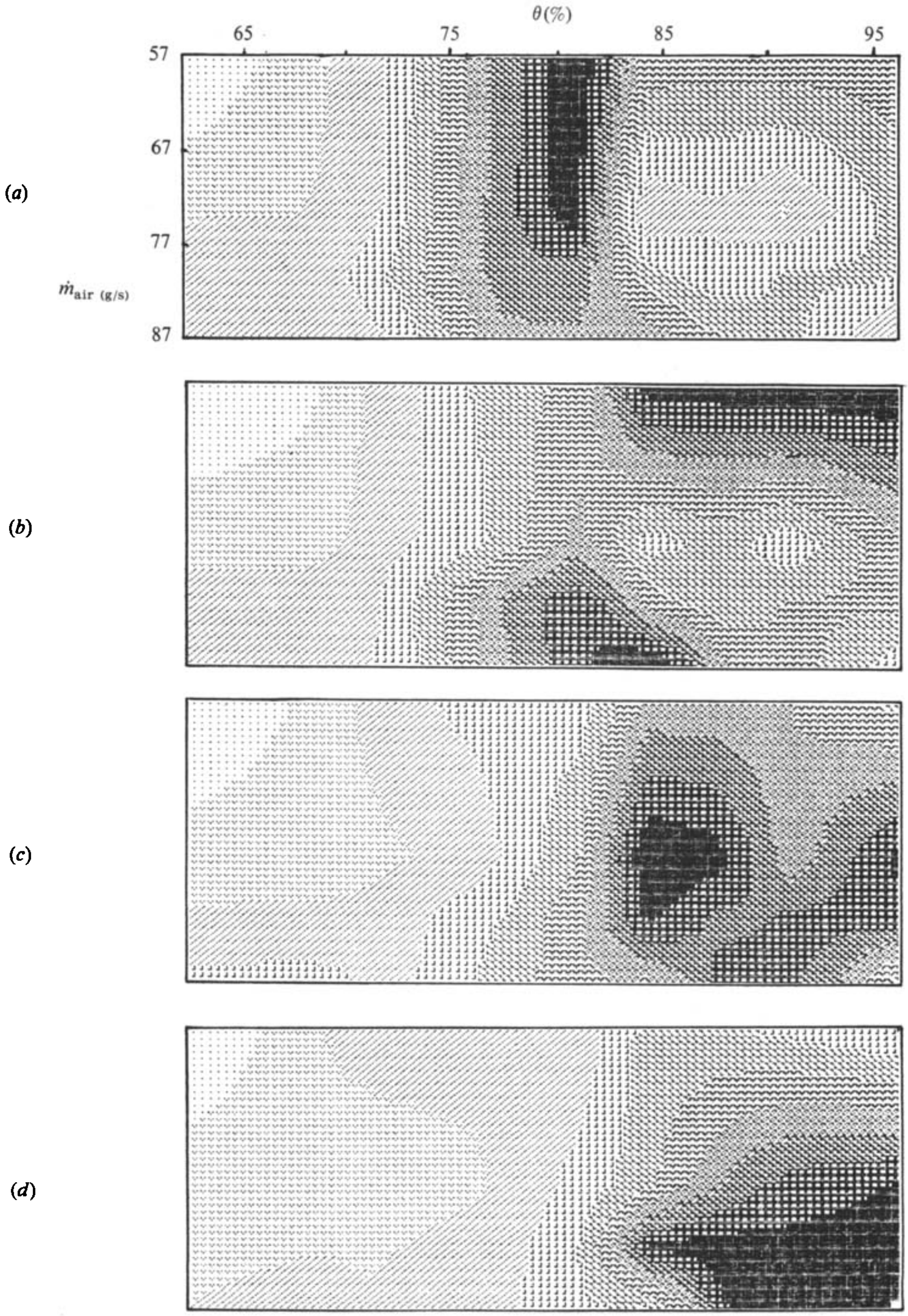

FIGURE 8. Acoustic spectral density levels in a specific frequency band plotted as a function of the operating parameters $\dot{m}_{\text{air}}$, Φ. The spectral amplitude is represented on a scale of grey levels. (*a*) Acoustic instability at 440 Hz. (*b*) 485 Hz. (*c*) 530 Hz. (*d*) 590 Hz.

Clearly, other frequencies would be obtained for combustion instabilities if fuel and oxydizer were changed (for example, if hydrogen and oxygen were used instead of propane and air).

Using a special data-base-signal processing method (see Darabiha *et al.* 1985) it is possible to determine the range of operating conditions which give rise to the various combustion oscillations. Figure 8 conveys this information. It gives the spectral density of the signal detected by microphone M_1 as a function of the operating conditions (air flow rate and equivalence ratio). Each map corresponds to one particular frequency band centred on the resonant frequencies 440, 485, 530 and 590 Hz. The spectral density in these bands is plotted on a scale of grey levels, thus delineating the range of occurrence of each oscillation. It is found that each mode occurs in a restricted domain of parameters. As the air flow rate and equivalence ratio are increased, there is a general trend towards higher acoustic intensities and frequencies. The frequency shifts are, however, discrete and the domains corresponding to each mode of oscillation are mutually exclusive.

A systematic investigation of the mean flame structures corresponding to the oscillatory combustion regimes indicates that the flow pattern is spatially periodic in the vicinity of the inlet plane. The jets of fresh mixture are isolated and parallel to the combustor axis. The reactive zone is more compact than in the stable situation.

When the combustor is operated in the most unstable regimes (i.e. at frequencies of 530 and 590 Hz) direct observations of the flame reveal some remarkable features. The central jet of fresh mixture appears as a dark straight strip parallel to the combustor axis (under stable conditions this jet bends upwards or downwards and interacts with one of the side jets).

The recirculation regions located behind the steps of the injection plane become luminous and emit in the blue, indicating the presence of chemical reactions. This is in sharp contrast with stable combustion situations. Many early studies (see Smith & Zukoski 1985, for a review) indicate that chemiluminescence, and hence chemical reaction, is almost absent in the recirculation zones formed behind the bluff bodies used to stabilize turbulent flames in ducts. This aspect is confirmed in the present experiments. Under stable operation the recirculation regions located behind the steps appear as dark zones and are essentially free of chemical reaction.

This experimental evidence already indicates that unstable oscillations may have a profound influence on the flow pattern and basic structure. The most remarkable feature is the change in behaviour of the recirculation region.

5.3. *Acoustic and hydrodynamic instabilities*

The unstable combustion regimes observed involve acoustic-wave oscillations. However, one cannot draw the conclusion that all instabilities of combustors with dump are acoustically coupled. In fact it is suggested by Bray *et al.* (1983) that the low-frequency 'buzz' instability arising in their ducted flame experiment is governed by hydrodynamic instabilities. Hydrodynamic instability theory is also used by Blackshear (1958) to explain the large-scale motions observed in his study.

To see if hydrodynamic instability contributes to the development of the unstable processes just described, let us estimate the frequency f_P of the most amplified mode of one of the jets of fresh mixture. This estimation is based on studies of isothermal shear flows. According to Ho & Huerre (1984) the Strouhal number characterizing the preferred mode of oscillation of two-dimensional jets is $St = f_P d/U_J \approx 0.25$, where U_J is the jet velocity and d the jet width at the nozzle. Here $d = 3\times10^{-3}$ m, the jet velocity $U_J \approx 40$ m/s, the preferred frequency f_P is about 3300 Hz, and the corresponding wavelength is $\lambda \approx 1$ cm. These rough estimates are confirmed by schlieren photographs taken under stable combustion. Hydrodynamic disturbances appearing on this view have a scale of the order of 1 cm (see figure 6). A preferred frequency f_P is also found in the range 3300–4000 Hz from time-resolved laser schlieren measurements.

Because the frequency f_P is 6–8 times greater than the observed frequencies it may be concluded that hydrodynamic instability does not play a major role in the process considered in this paper.

6. A vortex-driven acoustic instability

The most intense unstable regime, which appears at a frequency of 530 Hz, is now considered. In this regime, the power spectral density of microphone M_1 (figure 7) exhibits a sharp peak at this frequency, pressure signals are almost sinusoidal and allow conditional measurements and phase-average imaging. Spark schlieren photographs of the flame reveal the presence of large-scale vortices in the flow. The vortices form, grow in size, interact, burn and decay periodically. A typical cycle is shown in figure 9. The schlieren views composing this figure are obtained through the circular quartz windows of the combustor. The time interval separating successive views is $\Delta t = 0.23$ ms. The inlet plane is at the right of the window and the flow is directed from right to left.

At the first instant t_1 (figure 9*a*) the jet of fresh mixture is nearly straight and parallel to the combustor axis. The jet boundaries are blurred at the left side of the picture by residual fluctuations from the previous cycle. At the second moment t_2 (figure 9*b*) a corrugation develops on the central jet at about 1 cm from the inlet plane. Further downstream the sharp interface separating fresh mixture and burnt gases is fading and turbulent filaments from the wake of the previous vortex pattern are apparent.

At the next instant t_3 (figure 9*c*) the bulge has started to roll into a vortex. Wake filaments are still apparent in front of the vortex but most of the material in this region has reacted.

After another time interval, at time t_4 (figure 9*d*), the vortex has grown into a large 'mushroom' with a rounded cap. The vortices growing on the side jets become visible. Behind the cap a turbulent wake is formed.

At the next sampling time t_5 (figure 9*e*) the central and side vortices have grown in size and they interact strongly. Intense mixing, with production of small-scale turbulence, takes place in the interaction regions and in the vortex wake. A growing instability mode affects the central jet boundaries. While schlieren pictures cannot be used to distinguish between burning and non-burning gases it may be inferred that intense reactions are taking place in the interaction regions.

At the next instant t_6 (figure 9*f*) mixing and burning continue and extend over the whole vortex wake. The central jet develops a sinuous mode of hydrodynamic instability and the jet interface breaks into pieces.

After another sampling period, at moment t_7 (figure 9*g*), the gases surrounding the jet exhibit small-scale turbulence. The last portion of the jet is strongly perturbed and turbulent.

At time t_8 (figure 9*h*) the wake turbulence has decayed and the last portion has disappeared, leaving behind some filaments of unburned material.

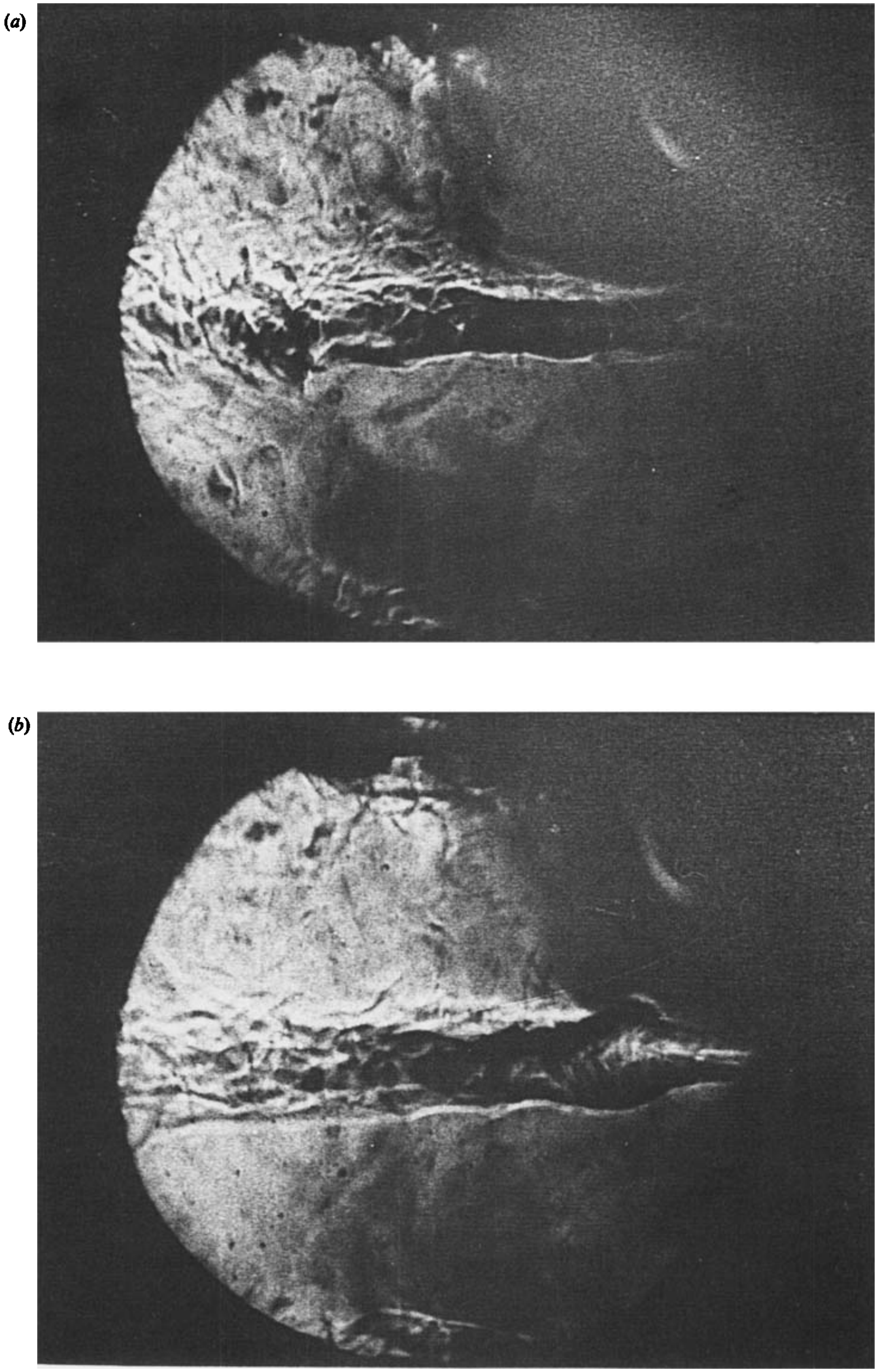

FIGURE 9(a, b). For caption see page 284.

(*c*)

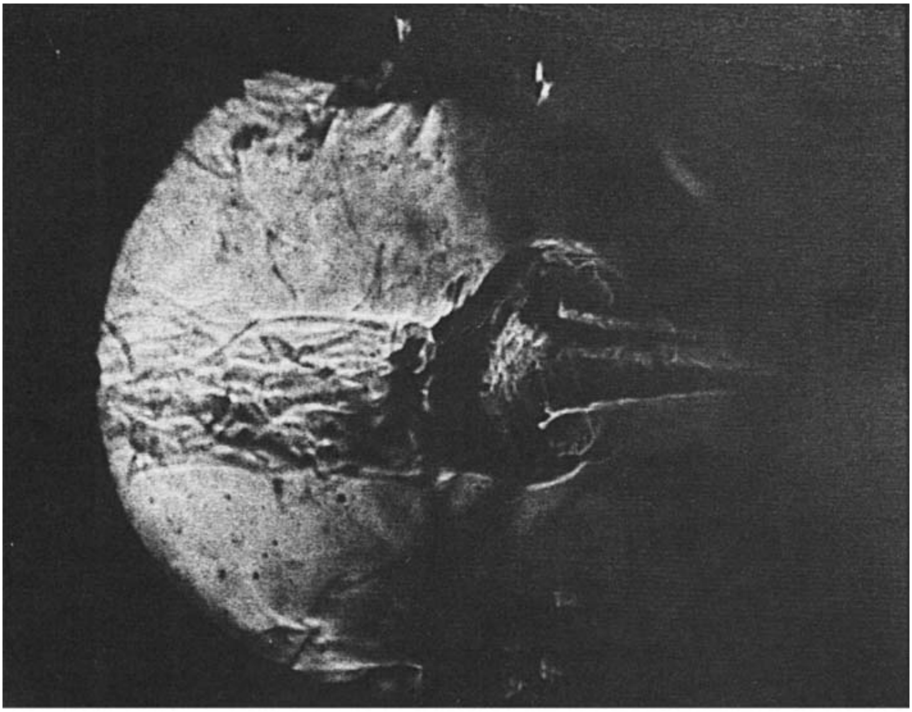

(*d*)

FIGURE 9(*c*, *d*). For caption see page 284.

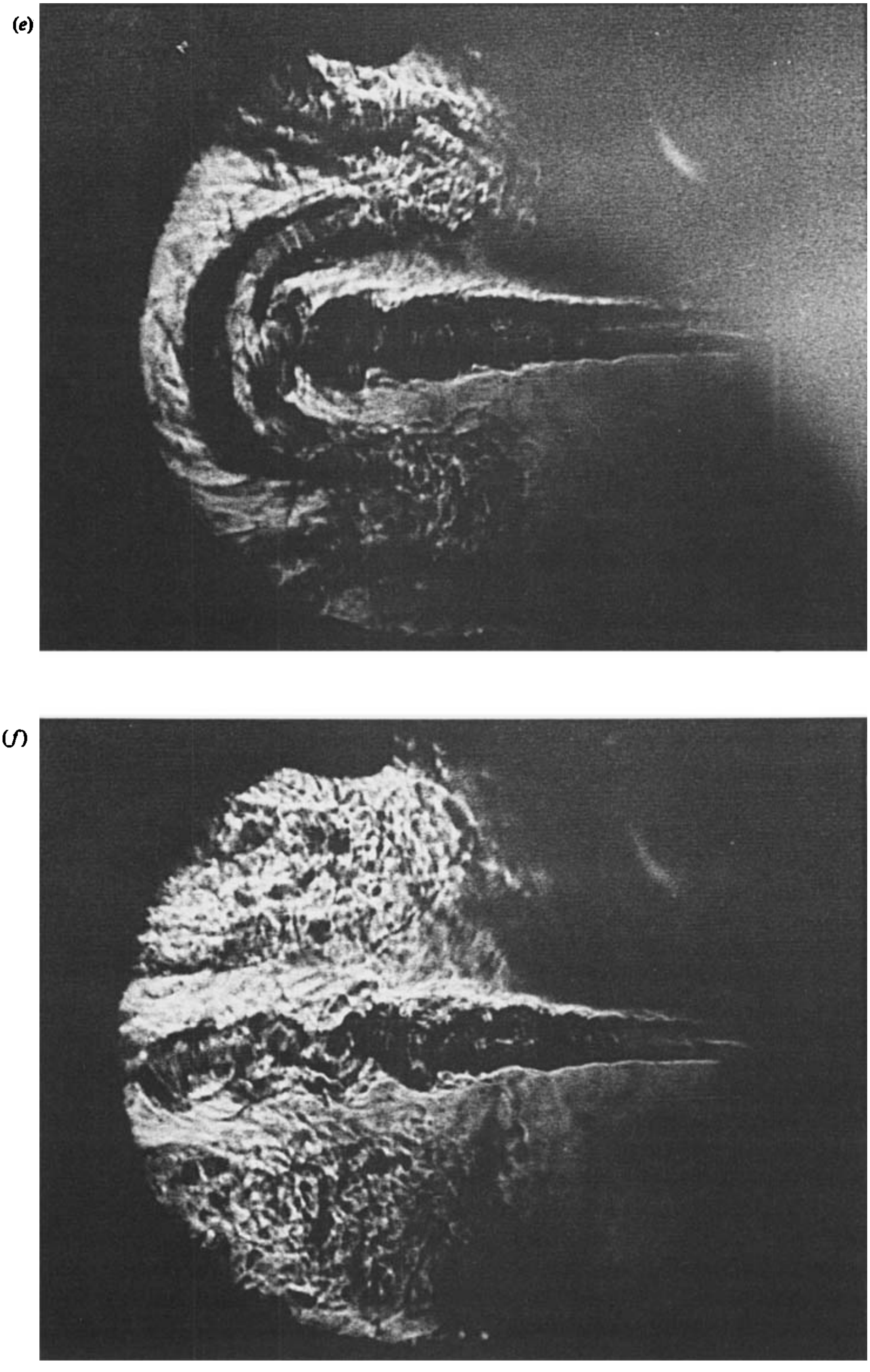

FIGURE 9 (*e*,*f*). For caption see page 284.

(g)

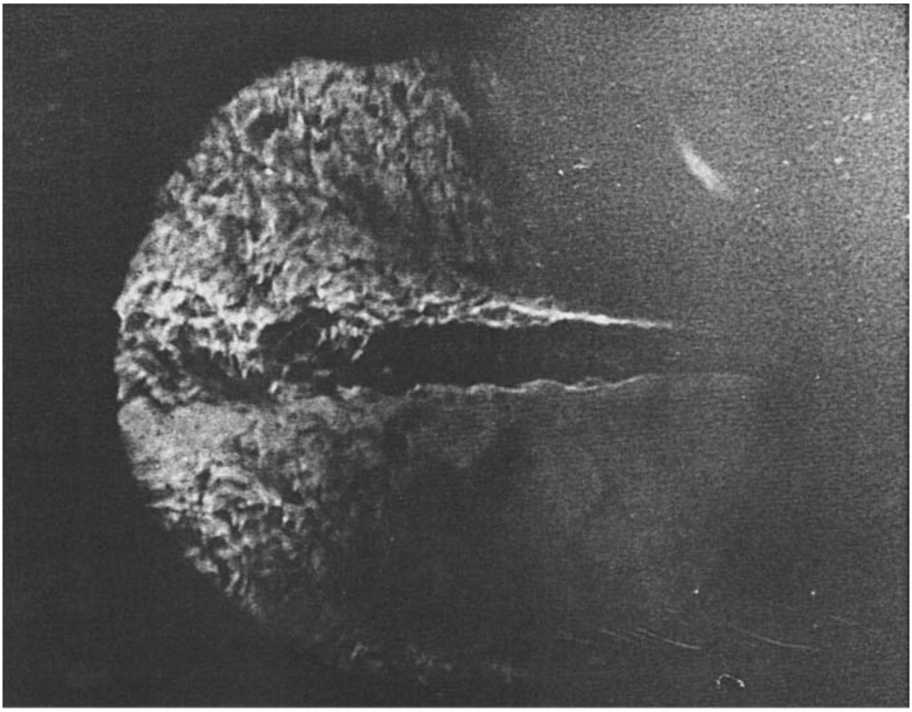

(h)

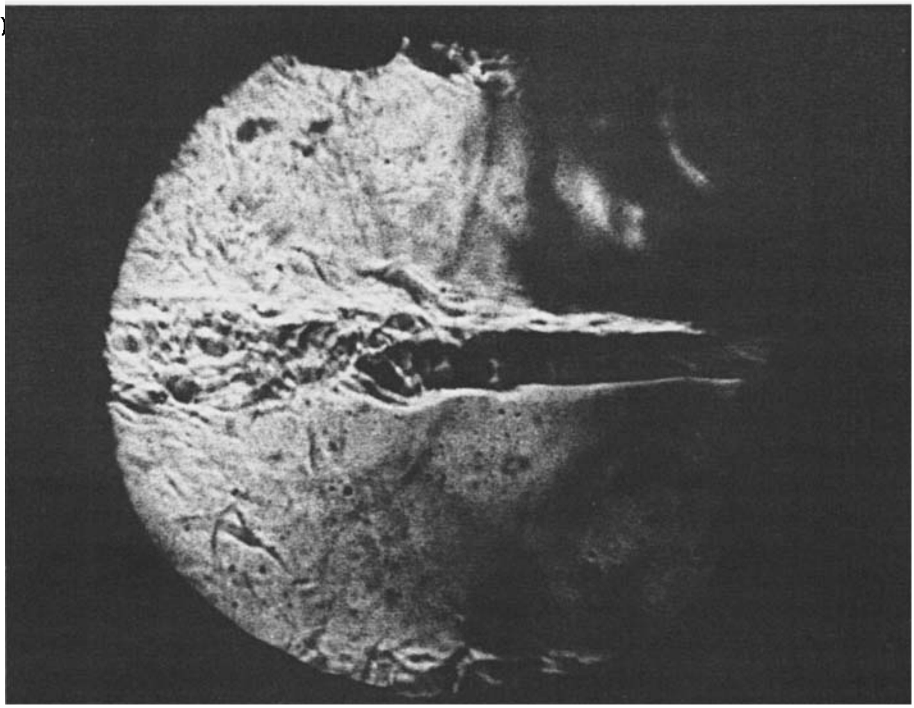

FIGURE 9(*g*, *h*). For caption see page 284.

(*i*)

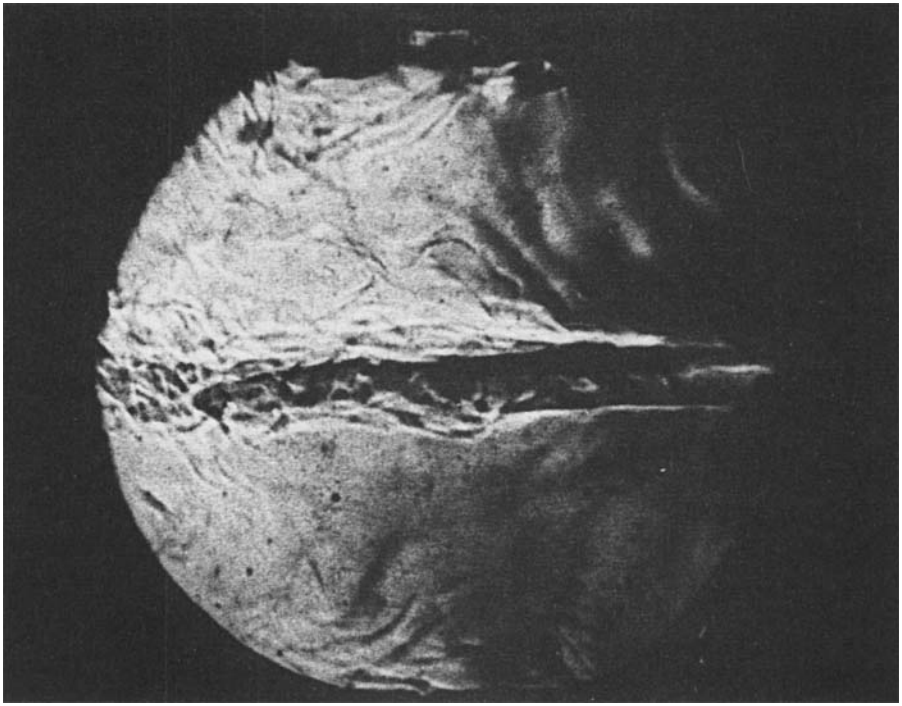

FIGURE 9. Spark-schlieren photographs of the central jet for the 530 Hz unstable regime. $\dot{m}_{\text{air}} = 73$ g/s, $\Phi = 0.92$. Time interval between frames: 0.23 ms. (*a*) t_1; (*b*) t_2; (*c*) t_3; (*d*) t_4; (*e*) t_5; (*f*) t_6; (*g*) t_7; (*h*) t_8; (*i*) t_9.

At time t_9 (figure 9*i*) the cycle is nearly completed ($t_9 - t_1 = 1.84$ ms, while the period of oscillation $T = 1/f \approx 1.88$ ms). The flow situation is similar to that observed at time t_1.

Let us now consider the C_2 emission maps composing figure 10. These maps provide phase-average images of the light intensity emitted by the C_2-radicals. As indicated in §3, this data may be interpreted as representative of the local heat-release source term. The phase-average light-intensity data samples are plotted on a scale of grey levels. The upper and lower limits of this scale are fixed to allow direct comparisons between images taken at various moments in the cycle. The darkest symbol in the scale represents the maximum light intensity while the lightest symbol corresponds to the minimum light emission.

At the initial moment t_1 (figure 10*a*) some light is radiated on the left of the window indicating that some residual burning takes place in the wake of the previous structure.

At the second moment t_2 (figure 10*b*) light emission is weak. Some light radiation takes place on the sides of the vortex corrugation. Another region of emission subsists at the left of the window and corresponds to the turbulent wake of the previous vortex structure.

At the next moment t_3 (figure 10*c*) four spots of light emission are made evident. The central spots appear on the sides of the central vortex displayed in figure 9(*c*). The side spots appear at the top and bottom borders of the viewing window and correspond to vortices developing on the side jets.

At time t_4 (figure 10*d*) the four spots have drifted towards the centre of the window and some coalescence begins between adjacent spots.

After another step in time, at t_5 (figure 10*e*), the emission of light takes place near the middle of the window. The light radiation is now more intense and the spots of the previous image have grown in size. The coalescence between adjacent spots produces an 8-shaped pattern.

After one more time step, at t_6 (figure 10*f*), the light emission reaches its maximum intensity. Active radiation takes place behind the vortex side branches, in the regions where the central vortex interacts with the side vortices and in the wakes of the vortex patterns.

Light emission continues at the next moment t_7 (figure 10*g*). Light radiation is strong over two broad spots. These spots are about at the same position as at the previous time step. This indicates that the burning material is being decelerated. Light emission is now also taking place over most of the window left side. In addition two small spots may be distinguished on the sides of the central jet. These spots correspond to burning in the strongly perturbed jet mixing layers.

At instant t_8 (figure 10*h*) burning proceeds in the wakes and in the central jet. The spots of light emission have slightly drifted to the left and the light intensity is weaker.

The cycle is nearly completed at t_9 (figure 10*i*). At that instant the light-emission pattern is nearly identical with that found at time t_1. The light intensity is weak indicating that most of the combustible material introduced during the cycle has essentially burned.

All emission images shown in figure 10 are slightly asymmetrical, with enhanced light radiation on the lower side of the window. This feature indicates that mixing and burning taking place below the central jet are more intense.

A comparison between the schlieren photographs and the C_2 radiation maps reveals additional features of the combustion process. From the photographs taken at instants t_4 and t_5 and from the corresponding radiation map it is clear that little combustion takes place on the vortex cap boundary. In this region the strain rate reaches high values. An estimate of this quantity may be obtained by calculating the average stretch factor $(1/A)\,(\mathrm{d}A/\mathrm{d}t)$ imposed on the cap during the initial growth of the structure. A direct measurement of the interfacial length indicates that the stretch factor is between 2×10^3 and $10^4\ \mathrm{s}^{-1}$. Such large values have the effect of nearly extinguishing any flame that would tend to develop at the vortex cap. The situation is in fact very close to that examined in some recent studies of premixed strained flames (see Libby & Williams 1982, 1983, 1984; and also Darabiha *et al.* 1986). It is shown there that when the premixed flame is highly strained it enters a regime of partial extinction.

Further evidence on the effect of high strain on the flame developing in a vortex is provided by recent experiments by Cattolica & Vosen (1984). From observations of laser-induced fluorescence, these authors show that the concentration of OH radicals is very low near the vortex cap and much larger in the side branches and wake where the flame develops.

Another interesting observation concerns the convection of the vortex patterns and the motion of the light-emitting regions. From the schlieren photographs one finds that the vortices are accelerated in the downstream direction at the moments t_2–t_5. The speed of the vortex cap is initially about 30 m/s and reaches 50 m/s at time t_5. Because the viewing window is too small it is, however, not possible to know what happens at later moments.

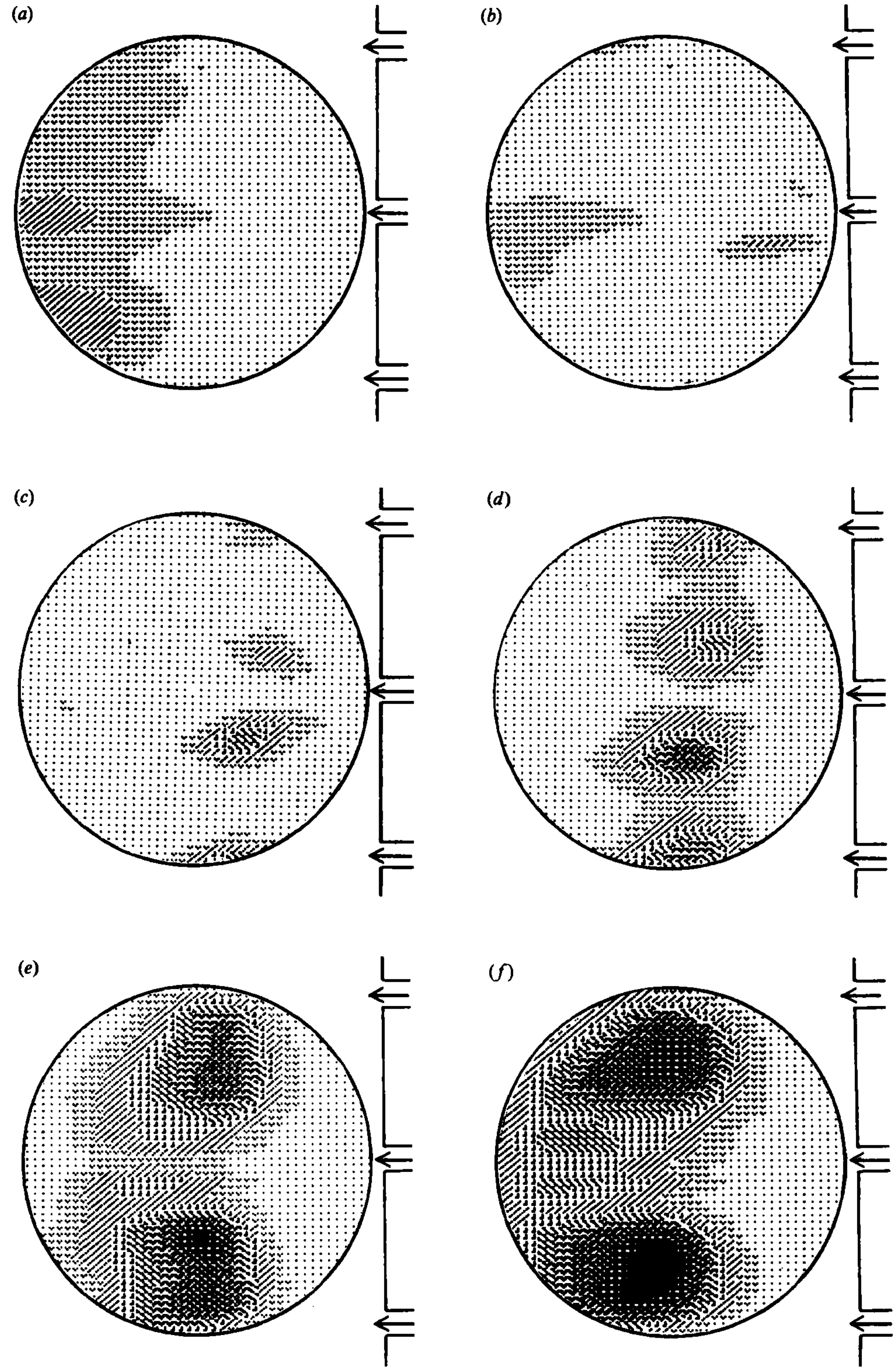

FIGURE 10(*a*,*f*). For caption see facing page.

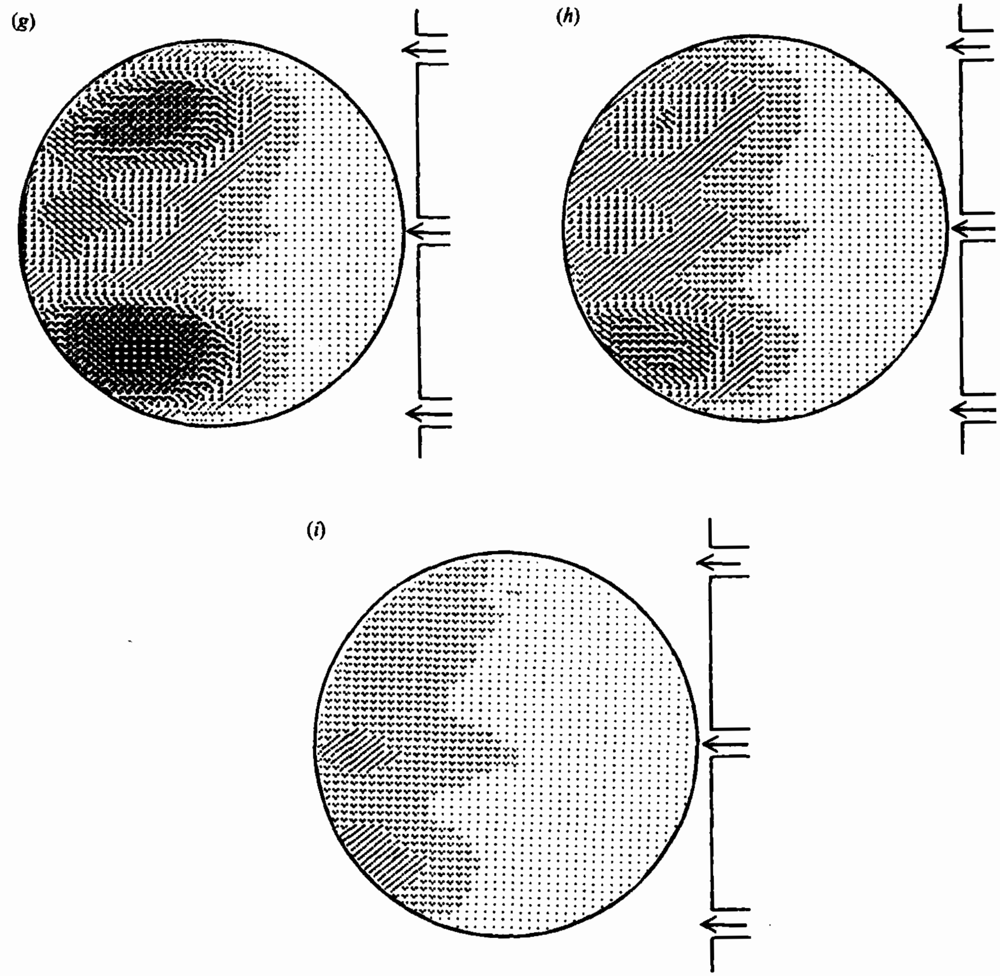

FIGURE 10. Instantaneous maps of the C_2-emission unsteady component for the 530 Hz unstable regime. $\dot{m}_{air} = 73$ g/s, $\Phi = 0.92$. Time interval between maps: 0.23 ms. (*a*)–(*i*) as for figure 9.

The convection of the light-emitting spots is more difficult to define because there is no clear boundary to follow. If one tracks the light-intensity maximum one finds that the velocity of this point decreases from 23 m/s at t_2 to 5 m/s at t_5, a sudden acceleration occurs between t_6 and t_7 and the velocity decreases again from 23 m/s at t_7 to 9 m/s at t_9. From these observations it may be concluded that the reaction zones trail behind the vortex patterns. The combustible material contained in the vortex structures escapes from the side branches and burns in the vortex wakes and interaction regions.

7. Vortex growth, heat release and acoustic oscillations

We now examine the relations between the acoustic cycle and the vortex shedding and burning processes. It is first important to locate the moments $t_1, \ldots, t_9$ with respect to the pressure and velocity fluctuations in the combustor. This will enable us to describe the full mechanism of instability.

Because a pressure measurement on the combustor is difficult we only use pressure data obtained at microphone M_1. This microphone is located on the test duct (see figure 1). The pressure signal detected by M_1 serves as a reference in the acquisition of the spark-schlieren and phase-average C_2-emission images. The same pressure signal is also used to deduce the pressure and velocity fluctuations at the combustor inlet plane. This information is obtained from the calculations presented in §4.

To begin this analysis it is worth looking at some implications of Rayleigh's criterion.This criterion is obtained from an acoustic energy balance of the reactive zone. It constitutes a classical tool in the analysis of acoustic instabilities and has been used in many different circumstances (see, for example, Putnam 1971). In the case of low-speed flows it is found that instability is locally amplified if the non-steady heat release $q'(\boldsymbol{x},t)$ and the pressure oscillation $p'(\boldsymbol{x},t)$ are in phase. More precisely let $G(\boldsymbol{x})$ designate the mean value of the product of these two quantities:

$$G(\boldsymbol{x}) = \frac{1}{T}\int_{[T]} q'(x,t)\,p'(x,t)\,\mathrm{d}t. \tag{13}$$

Then, local amplification occurs if $G(\boldsymbol{x}) > 0$, while damping corresponds to $G(\boldsymbol{x}) < 0$.

If one considers the acoustic energy balance for the combustor cavity one must integrate the local Rayleigh index $G(\boldsymbol{x})$ over the combustor volume:

$$\overline{G} = \frac{1}{V}\int_V G(\boldsymbol{x})\,\mathrm{d}V = \frac{1}{VT}\int_V\int_{[T]} q'(\boldsymbol{x},t)\,p'(\boldsymbol{x},t)\,\mathrm{d}t\,\mathrm{d}V. \tag{14}$$

If the losses of acoustic energy from the cavity are small, it is expected that the global Rayleigh index $\overline{G}$ will be nearly equal to zero.

To use (14) it is in principle necessary to have a complete knowledge of the distributions of $q'(\boldsymbol{x},t)$ and $p'(\boldsymbol{x},t)$ over the whole volume of the cavity.

Such information is out of reach. However, an estimate of $\overline{G}$ may be obtained if a 'compactness' assumption is used. This assumption is justified if the wavelength λ greatly exceeds the length δ_R of the reaction zone. This is certainly the case, since $\lambda \approx 0.9$ m while $\delta_R \approx 0.05$ m. Then, the pressure oscillation at one instant in time $p'(\boldsymbol{x},t)$ is nearly constant over the reaction zone and because this zone is adjacent to the inlet plane, $p'(\boldsymbol{x},t)$ may be assimilated to the pressure fluctuation at the inlet plane:

$$p'(\boldsymbol{x},t) \approx p'(\boldsymbol{x}_0,t).$$

Then the global Rayleigh index may be expressed as

$$\overline{G} = \frac{1}{VT}\int_{[T]} p'(\boldsymbol{x}_0,t)\int_V q'(\boldsymbol{x},t)\,\mathrm{d}t\,\mathrm{d}V. \tag{15}$$

If we now define the global non-steady heat release by

$$Q'(t) = \int_V q'(\boldsymbol{x},t)\,\mathrm{d}V, \tag{16}$$

the global Rayleigh index may be written in the final form

$$\overline{G} = \frac{1}{VT}\int_{[T]} p'(\boldsymbol{x}_0,t)\,Q'(t)\,\mathrm{d}t. \tag{17}$$

From this development, it appears that the quantities of interest are the pressure fluctuation at the inlet plane and the global non-steady heat release. To obtain $Q'(t)$ we use the C_2-emission intensity integrated over the combustor window. This is a

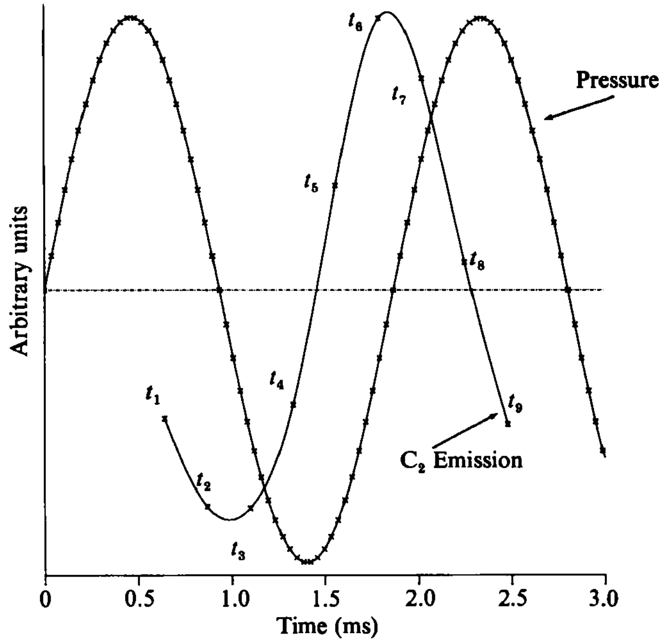

FIGURE 11. Computed pressure cycle at the inlet plane and global C_2 radiation fluctuations in the combustor for the 530 Hz unstable regime. $\dot{m}_{\text{air}} = 73$ g/s, $\Phi = 0.92$.

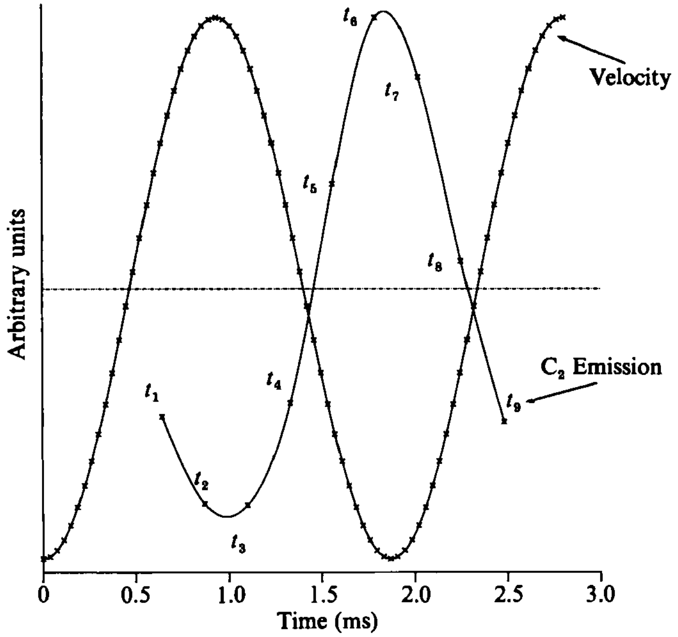

FIGURE 12. Computed velocity cycle at the inlet plane and global C_2 radiation fluctuations in the combustor for the 530 Hz unstable regime. $\dot{m}_{\text{air}} = 73$ g/s, $\Phi = 0.92$.

suitable approximation because most of the non-steady combustion takes place in the region covered by the viewing window: combustion in the vortices is almost completed when they are convected out of the window (see figure 10*h*).

The variations of $p'(x_0, t)$ and $Q'(t)$ are displayed in figure 11. The pressure and global heat-release signals are nearly in quadrature and the global Rayleigh criterion $\bar{G} \approx 0$ is verified. It is worth underlining that this feature is characteristic of combustion oscillations if the losses of acoustic energy from the combustor are small. A similar conclusion may be reached from the results published by Smith & Zukoski (1985).

Figure 11 indicates how burning takes place in the vortices during a pressure cycle. It is also of interest to see how these vortices are formed. The velocity fluctuation at the inlet plane certainly plays a role in the vortex-shedding process. Figure 12 displays this quantity and the global non-steady heat release. The moments $t_1, \ldots, t_9$ corresponding to the schlieren and phase-average images are also indicated. At instant t_2 the vortex forms and appears as a corrugation of the central jet (figure 9*b*). This moment corresponds to a nearly maximum value of the velocity fluctuation. The vortex formation appears as the consequence of a large positive excursion of the velocity. The time lag between the pressure oscillation maximum and the vortex-formation instant is about $\frac{1}{4}T$.

Once formed, the vortex cap is accelerated by the acoustic velocity fluctuation up to time t_4. This acceleration continues beyond t_4. The velocity fluctuation is negative but a large volumetric expansion is produced by combustion at times t_4–t_6. The volume expansion due to heat release also contributes to the velocity reversal at the flame holder.

The time lag between the vortex formation and the maximum heat release is about $\frac{1}{2}T$. Consequently the time delay between the pressure and heat release maxima is $\frac{3}{4}T$. In terms of phase the global heat-release maximum occurs at $\frac{3}{2}\pi$ after a positive pressure maximum.

8. Conclusion

This paper describes the acoustical and fluid-mechanical aspects of combustion instability in a multiple-flame-holder dump combustor. Acoustic modes are calculated and the feedback process involved in the instability is identified. It is shown that the low-frequency oscillations of the combustor are acoustically coupled and that the frequencies of the main modes may be predicted by a simple one-dimensional wave analysis of the system.

Fluid-mechanical processes are examined with spark-schlieren and phase-average images of C_2 emission. These two diagnostics indicate that certain instabilities are vortex driven. From the information collected it is possible to propose a mechanism for this type of instability.

Vortex shedding occurs when the velocity fluctuation at the inlet plane is positive and reaches its maximum. The vortex is convected downstream and grows in size. Vortices formed on neighbouring jets interact producing small-scale turbulence and intense mixing. The non-steady heat release reaches its maximum at that time. This occurs when the pressure fluctuation becomes positive. The global fluctuation of heat release lags the pressure oscillation at the inlet plane by about $\frac{3}{4}T$.

In this way the global Rayleigh criterion for the cavity is satisfied. With respect to a positive pressure maximum, the vortex formation takes about $\frac{1}{4}T$ and its growth and combustion takes another $\frac{1}{2}T$. The non-steady heat released feeds energy into the acoustic wave allowing the shedding of a new vortex at the next positive acoustic velocity maximum. It is also found that the acoustic field accelerates the vortex during its initial growth. After a certain time this acceleration is produced by the volume expansion due to heat release.

These results suggest that the three main features which govern vortex-driven instabilities are:

(i) vortex shedding and its relation to strong velocity oscillations;

(ii) convection, acceleration and combustion of the vortex. In the case of multiple flamesheets it is important to understand how combustion evolves when neighbouring vortices interact;

(iii) influence of the non-steady heat sources on the acoustic velocity field in the system.

It is now possible to infer that the processes described in this paper occur in many practical situations.

We wish to acknowledge helpful discussions with Professors Frank Marble and Edward Zukoski of the California Institute of Technology. A number of figures were generated with the CATIA software on an IBM 4341 computer made available to us by the IBM Co. This study is financially supported by a DRET contract monitored by Jacques Besnault.

REFERENCES

BARRERE, M. & WILLIAMS, F. A. 1968 Comparison of combustion instabilities found in various types of combustion chambers. *Twelfth Symp. (Intl) on Combustion*, p. 169. The Combustion Institute, Pittsburgh.

BLACKSHEAR, P. L. 1958 Growth of disturbances in a flame generated shear region. *NACA Rep.* 1360.

BRAY, K. N. C., CAMPBELL, I. G., LEE, O. K. L. & MOSS, J. B. 1983 An investigation of reheat buzz instabilities. *Aeronautics and Astronautics, AASU Memo* 83/2. University of Southampton.

CATTOLICA, R. S. & VOSEN, S. R. 1984 Two-dimensional fluorescence imaging of a flame-vortex interaction. *Sandia Rep.* Sand 84-8704.

DARABIHA, N. 1984 Un modèle de flamme cohérente pour la combustion prémélangée: analyse d'un foyer turbulent à élargissement brusque. Doctoral thesis, Ecole Centrale des Arts et Manufactures, Chatenay-Malabry, France.

DARABIHA, N., CANDEL, S. M. & MARBLE, F. E. 1986 The effect of strain rate on a premixed laminar flame. *Combust. Flame* **64**, 203.

DARABIHA, N., POINSOT, T., CANDEL, S. M. & ESPOSITO, E. 1986 A correlation between flame structures and acoustic instabilities. *Presented at the tenth ICODERS, Berkeley 1985. Progress in Astronautics and Aeronautics*, AIAA, pp. 283–295.

HAARJE, D. T. & REARDON, F. M. 1972 Liquid propellant rocket combustion instability. *NASA SP* 194.

HO, C. M. & HUERRE, P. 1984 Perturbed free shear layers. *Ann. Rev. Fluid Mech.* **16**, 365.

HURLE, I. R., PRICE, R. B., SUGDEN, T. M. & THOMAS, A. 1968 Sound emission from open turbulent premixed flames. *Proc. R. Soc. Lond.* A **303**, 409.

JOHN, R. R. & SUMMERFIELD, M. 1957 Effect of turbulence on radiation intensity from propane-air flames. *Jet Propulsion* **27**, 169.

JOHN, R. R., WILSON, E. S. & SUMMERFIELD, M. 1955 Studies of the mechanism of flame stabilization by a spectral intensity method. *Jet Propulsion* **25**, 535.

KELLER, J. O., VANEVELD, L., KORSCHELT, D., HUBBARD, G. L., GHONIEM, A. F., DAILY, J. W. & OPPENHEIM, A. K. 1981 Mechanism of instabilities in turbulent combustion leading to flashback. *AIAA J.* **20**, 254.

LIBBY, P. A. & WILLIAMS, F. A. 1982 Structure of laminar flamelets in premixed turbulent flames. *Combust. Flame* **44**, 287.

LIBBY, P. A. & WILLIAMS, F. A. 1983 Strained premixed laminar flames under non-adiabatic conditions. *Combust. Sci. Technol.* **31**, 1.

LIBBY, P. A. & WILLIAMS, F. A. 1984 Strained premixed laminar flames with two reaction zones. *Combust. Sci. Technol.* **37**, 221.

PARKER, L. J., SAWYER, R. F. & GANJI, A. R. 1979 Measurement of vortex frequencies in a lean, premixed, prevaporized combustor. *Combust. Sci. Technol.* **20**, 235.

PITZ, R. W. & DAILY, J. W. 1981 Experimental study of combustion in a turbulent free shear layer formed at a rearward facing step. *Nineteenth Aerospace Sciences Meeting, St Louis, Missouri.* AIAA. Paper no. 0106.

PUTNAM, A. A. 1971 *Combustion Driven Oscillations in Industry*. Elsevier.

ROGERS, D. E. & MARBLE, F. E. 1956 A mechanism for high frequency oscillations in ramjet combustors and afterburners. *Jet Propulsion* **26**, 456.

SMITH, D. A. & ZUKOSKI, E. E. 1985 Combustion instability sustained by unsteady vortex combustion. *Twenty-first Joint Propulsion Conference, Monterey, California.* AIAA/SAE/ASME/ASEE. Paper no. 1248.

WILLIAMS, F. A. 1985 *Combustion Theory*, 2nd edn. Benjamin Cummings.

YAMAGUCHI, S., OHIWA, N. & HASEGAWA, T. 1985 Structure of blow-off mechanism of rod-stabilized premixed flame. *Combust. Sci. Technol.* **62**, 31.